Analytical Prediction for Electromagnetic Characteristics of Tubular Linear Actuator with Halbach Array Using Transfer Relations

Seok-Myeong Jang* and Jang-Young Choi†

Abstract – This paper deals with analytical prediction for electromagnetic characteristics of a tubular linear actuator with Halbach array using transfer relations, namely, Melcher's methodology. Using transfer relations derived in terms of magnetic vector potential and a two-dimensional (2-d) cylindrical coordinate system, this paper derives analytical solutions for magnetic vector potential due to permanent magnets (PMs) and stator winding currents. On the basis of these analytical solutions, this paper also achieves analytical solutions for the magnetic fields distribution produced by PMs, stator windings current and axial thrust. The analytical results are validated extensively by finite element (FE) analyses. In particular, test results such as thrust measurements are given to confirm the analysis. Finally, this paper estimates control parameters using analytical solutions and test results such as thrust, back-emf, inductance and resistance measurements.

Keywords: Control Parameters, Transfer Relations, Tubular Linear Actuator

1. Introduction

Linear motion machines are being employed increasingly in applications ranging from transportation, manufacturing, and office automation to material processing, health care, and generation systems. Particular examples include stirling cycle cryogenic coolers, generators and artificial heart devices. The advantages of such a motor is good linearity and it does not require mechanical energy conversion parts that change rotary motion into linear motion, such as screws, gears and chains. It is notable that the absence of these mechanical counterparts results in a higher dynamic performance, improved reliability and reduced power loss due to mechanical friction [2-3]. In addition, tubular linear machines are very attractive compared to flat linear machines because they produce high thrust due to the high PM's coefficient of utilization and don't have end turn effects. Because of these advantages, tubular linear PM machines become an attractive candidate for many industry applications, in spite of such disadvantages as difficulty in manufacturing a permanent magnet mover, maintaining fixed air-gap length and laminating for reducing eddy current loss.

Wang [2] presented analytical solutions for open-circuit field, armature reaction field distribution of tubular linear machines with radially, axially and Halbach magnetized PMs by using magnetic vector potential, and predicted the thrust by employing the Lorentz force equation, which is very reliable but contains integrals of Bessel functions that cause a significant analytical burden. Kim [4] also performed analysis and design of the tubular linear motor that has an air-cored and inner 3-phase stator winding and the outer Halbach array mover without back iron, by using Melcher's methodology, namely, transfer relations. In particular, he employed the Maxwell stress tensor applied to planar motor given in [5] for the prediction of thrust. Although the Maxwell stress tensor applied to planar motor is employed in tubular geometry, this method is reasonable and is free from integrals of the Bessel functions. Moreover, the analytical techniques, namely, transfer relations presented in [4] can be easily adapted to the tubular linear actuator shown in Fig. 1 that has an iron-cored and outer single-phase stator winding and the inner Halbach array mover with back iron, by changing boundary conditions properly and by performing a current density modeling of the single-phase winding.

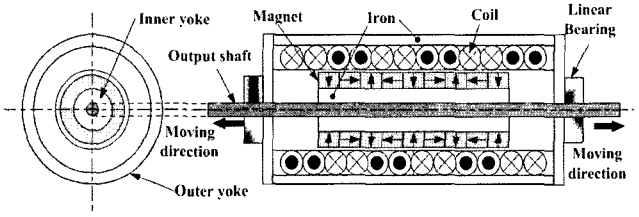

Fig. 1. Schematic of tubular linear actuator.

Therefore, this paper derives the generalized vector potentials due to the PMs and single-phase winding currents using the transfer relations. And then, analytical

† Corresponding Author: Dept. of Electrical Engineering, Chungnam National University, Korea. (aramis76@cnu.ac.kr)
* Dept. of Electrical Engineering, Chungnam National University, Korea. (smjang@cnu.ac.kr)
Received 1 April, 2006 ; Accepted 2 November, 2006

solutions for magnetic field distributions due to PMs and stator winding currents and the thrust of the tubular linear actuator are obtained from those. Analytical results compare well with corresponding FE predictions. In particular, test results such as thrust measurements according to position of the mover are given to confirm the analysis. Finally, on the basis of 2-d analytical solutions and test results, control parameters of the tubular linear actuator are estimated.

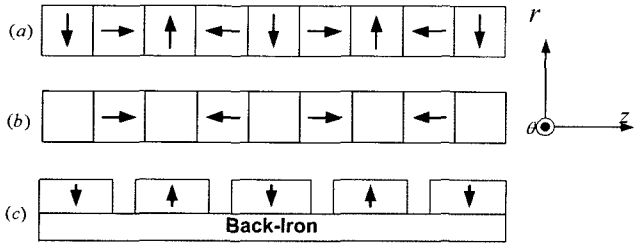

Fig. 2. Typical arrangements of PMs in a tubular linear actuator: (a) Halbach, (b) axial and (c) radial magnetization.

2. Structures of tubular linear actuator

Fig. 1 shows the structure of the tubular linear actuator, which consists of the PMs as a mover, a coil-wrapped hollow bobbin and iron core as a pathway for magnet flux. As will be discussed in following sections, we choose Halbach array as the mover and slotless structure as a stator.

2.1 PM array as a mover

Fig. 2 (a), (b) and (c) show the Halbach magnetized, axially magnetized and radially magnetized mover for the tubular linear actuator, respectively. In particular, the Halbach magnetized mover has inherent self shielding property, and thereby does not require a back iron. The axially magnetized mover likewise does not need one for the magnetic path, while the radially magnetized mover comprises array surface-mounted PM blocks on an iron backing. Moreover, the fundamental field of the Halbach array is stronger by 1.4 than that of a conventional array, and thus the power efficiency of the motor with Halbach array is doubled. The magnetic field of the Halbach array is more purely sinusoidal than that of the others, resulting in a simple control structure [6]. These advantages are what made us choose the Halbach array as the mover of the tubular linear actuator.

2.2 The type of stator structures

Stator structures of electric machines are widely classified into two types; one is slotted stator, the other is slotless stator. The former usually has a higher force density, but may also produce an undesirable destabilizing tooth ripple cogging force and have the highest eddy current loss in the magnets and the iron, in particular when operating at high speed. On the other hand, the latter eliminates the tooth ripple cogging effect, and thereby improves the dynamic performance at the expense of a reduction in specific force capability [2]. Therefore, this paper chooses slotless structure as the stator of the tubular linear actuator. Although this design choice sacrifices the higher force capabilities that would be possible with iron slots in the stator in favor of smooth actuation, with the advent of the modern high-energy rare-earth PMs and employment of the Halbach array, slotless motor topologies have become interesting solutions [7].

3. Analytical model and transfer relations

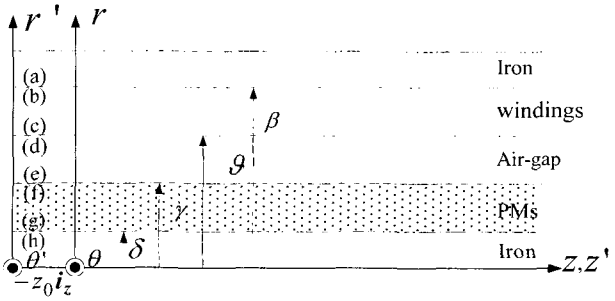

Fig. 3. The simplified analytical model.

Fig. 3 shows the simplified analytical model of the tubular linear actuator shown in Fig. 1. As indicated in Fig. 3, the PM regions carry a primed coordinate frame that is displaced from the base coordinate frame by a vector $-z_0 \boldsymbol{i}_z$. Here z_0 is the lateral displacement of the PMs relative to the stator. Letters (a)-(h) represent the surfaces at the indicated boundaries and Greek letters δ-β denote the inner and outer radii of the PMs and the stator. In order to obtain the field solutions, this paper assumes that the permeability of the stator core and the mover shaft is infinite. The relative recoil permeability of winding and PM regions are also assumed to be unified. On the other hand, the Fourier series expansion for the magnetization of the Halbach array is represented as

$$\boldsymbol{M} = \sum_{n=-\infty}^{\infty} \left[G(r) M_{rn} \boldsymbol{i}_{r'} + M_{zn} \boldsymbol{i}_{z'} \right] e^{-jk_n z'} \tag{1}$$

where the pole pitch of the actuator is τ, and the spatial wave-number of the nth harmonic is $k_n = n\pi/\tau$. G(r) makes radial components of the Halbach magnetization function for both radial and axial coordinates without decrease of

accuracy for magnetization quantity and is given by [8]

$$G(r)=\frac{c_1}{r}+c_2 r,\quad c_1=\frac{\gamma\delta}{\gamma+\delta}\quad\text{and}\quad c_2=\frac{1}{\gamma+\delta} \tag{2}$$

The complex Fourier coefficients of nth-order radial and axial magnetization components, namely, M_{rn} and M_{zn} are given by

$$M_{rn}=\frac{B_{rem}}{jn\pi\mu_0}\left\{e^{jn\pi\alpha/2}-e^{-jn\pi\alpha/2}\right\}$$
$$M_{zn}=\frac{B_{rem}}{j2n\pi\mu_0}\left\{\left(e^{-jn\pi}-1\right)e^{jn\pi\alpha/2}+\left(e^{jn\pi}-1\right)e^{-jn\pi\alpha/2}\right\} \tag{3}$$

where B_{rem} and μ_0 denote the remanence of PMs and the permeability of the air, respectively. $\alpha = \tau_m/\tau$; τ_m is the PM width. In a similar manner, the Fourier series expansion for current density of slotless stator windings is expressed as

$$\boldsymbol{J}=\sum_{n=-\infty}^{\infty}H(r)J_n e^{-jk_n z}\boldsymbol{i}_\theta \tag{4}$$

where J_n is the nth-order complex Fourier coefficient for current density and is given by

$$J_n=-\frac{2J_0}{jn\pi}\left\{e^{-jn\pi/2}-e^{-j3n\pi/2}\right\} \tag{5}$$

where the amplitude of current density J_0 is given by

$$J_0=\frac{Ni_s}{\tau(\beta-\vartheta)} \tag{6}$$

where N and i_s are the turns per pole and winding current, respectively. H(r) is also given by

$$H(r)=\frac{c_3}{r}+c_4 r,\quad c_3=\frac{\vartheta\beta}{\beta+\vartheta}\quad\text{and}\quad c_4=\frac{1}{\beta+\vartheta} \tag{7}$$

Next, the transfer relations which relate the fields evaluated at the surfaces identified in the model of Fig. 3 are [4]

$$\begin{bmatrix}B_{zn}^f\\B_{zn}^g\end{bmatrix}=-k_n^2\begin{bmatrix}F_0(\delta,\gamma) & G_0(\gamma,\delta)\\G_0(\delta,\gamma) & F_0(\gamma,\delta)\end{bmatrix}\begin{bmatrix}A_{\theta n}^f\\A_{\theta n}^g\end{bmatrix} - j\mu_0 k_n M_{rn}\begin{bmatrix}F_0(\delta,\gamma)+G_0(\gamma,\delta)\\G_0(\delta,\gamma)+F_0(\gamma,\delta)\end{bmatrix} \tag{8}$$

$$\begin{bmatrix}B_{zn}^d\\B_{zn}^e\end{bmatrix}=-k_n^2\begin{bmatrix}F_0(\gamma,\vartheta) & G_0(\vartheta,\gamma)\\G_0(\gamma,\vartheta) & F_0(\vartheta,\gamma)\end{bmatrix}\begin{bmatrix}A_{\theta n}^d\\A_{\theta n}^e\end{bmatrix} \tag{9}$$

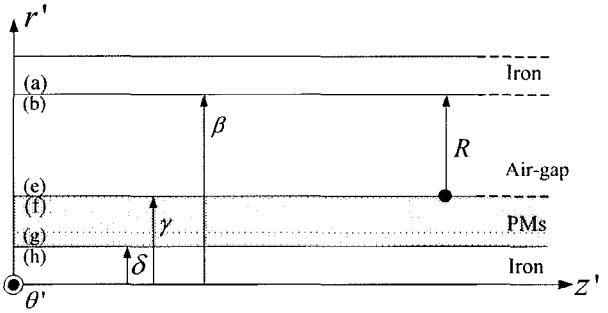

Fig. 4. Model for the generalization of vector potentials due to PMs.

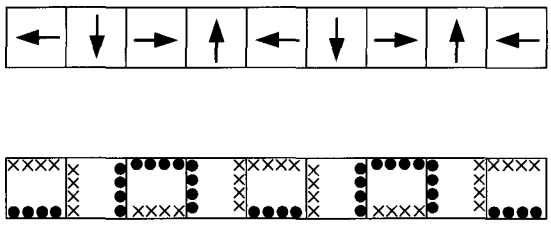

Fig. 5. Electromagnetic dual of cylindrical Halbach array: (a) Halbach magnet array and (b) equivalent current model.

$$\begin{bmatrix}B_{zn}^b\\B_{zn}^c\end{bmatrix}=-k_n^2\begin{bmatrix}F_0(\vartheta,\beta) & G_0(\beta,\vartheta)\\G_0(\vartheta,\beta) & F_0(\beta,\vartheta)\end{bmatrix}\begin{bmatrix}A_{\theta n}^b\\A_{\theta n}^c\end{bmatrix} + \mu_0 J_n\begin{bmatrix}F_0(\vartheta,\beta)+G_0(\beta,\vartheta)\\G_0(\vartheta,\beta)+F_0(\beta,\vartheta)\end{bmatrix} \tag{10}$$

The geometric parameters $F_0(x,y)$ and $G_0(x,y)$ are [4]

$$F_0(x,y)=-\frac{I_1(k_n x)K_0(k_n y)+K_1(k_n x)I_0(k_n y)}{k_n\{I_1(k_n y)K_1(k_n x)-K_1(k_n y)I_1(k_n x)\}} \tag{11}$$

and

$$G_0(x,y)=-\frac{1}{k_n^2 x\{I_1(k_n y)K_1(k_n x)-K_1(k_n y)I_1(k_n x)\}} \tag{12}$$

where I_1 and K_1 are modified Bessel functions of the first and second kind, of order one whiles I_0 and K_0 are also modified Bessel functions of the first and second kind, of order zero. Equations (8), (9) and (10) describe the transfer relations in the PM, air-gap and stator winding regions,

respectively. It is noted that the axial magnetization of the Halbach array, namely, M_{zn} which does not appear in (8) will be considered in boundary conditions. It is also noted that the source terms of (8) and (10) presented in this paper are different from those of (7) and (9) presented in [4] because the function G(r) and H(r) introduced by this paper are 1 at lower and upper boundaries of regions containing source terms.

4. Fields due to PMs

4.1 Boundary conditions

By assumption that the relative recoil permeability of the winding regions is unity, winding regions is contained in air-gap regions, as shown in Fig. 4, for the case when the magnetic field distributions due to PMs are analyzed. On the other hand, Halbach magnet array shown in Fig. 5(a) can be expressed as equivalent current model by applying Ampere's law to it, as shown in Fig. 5(b). Since the equivalent current for axial components of the Halbach magnetization exists at lower and upper surface of the PMs, it must be considered in boundary conditions. As a consequence, boundary conditions used in prediction of the magnetic field distributions due to PMs are as follows:

i) $B_{zn}^{b}=0$ and $B_{zn}^{h}=0$ by assumptions that the permeability of the stator core and rotor shaft is infinite,

ii) $B_{zn}^{e}-B_{zn}^{f}=\mu_0 M_{zn}$ and $B_{zn}^{g}-B_{zn}^{h}=-\mu_0 M_{zn}$ because the equivalent current of axial magnetization for Halbach array is existed at upper and lower surface of PMs,

iii) $A_{\theta n}^{e}=A_{\theta n}^{f}$ and $A_{\theta n}^{g}=A_{\theta n}^{h}$ by continuity of vector potentials at all boundaries.

4.2 Vector potentials

By boundary conditions ii) and iii) presented in section 4.1, (8) can be rewritten by

$$\begin{bmatrix} B_{zn}^{e} \\ B_{zn}^{h} \end{bmatrix} = -k_n^2 \begin{bmatrix} F_0(\delta,\gamma) & G_0(\gamma,\delta) \\ G_0(\delta,\gamma) & F_0(\gamma,\delta) \end{bmatrix} \begin{bmatrix} A_{\theta n}^{e} \\ A_{\theta n}^{h} \end{bmatrix} + \begin{bmatrix} N_1 \\ N_2 \end{bmatrix} \quad (13)$$

As shown in Fig. 4, since the air-gap regions contain the winding regions, the transfer relations of air-gap regions shown in Fig. 4 are given by

$$\begin{bmatrix} B_{zn}^{b} \\ B_{zn}^{e} \end{bmatrix} = -k_n^2 \begin{bmatrix} F_0(\gamma,\beta) & G_0(\beta,\gamma) \\ G_0(\gamma,\beta) & F_0(\beta,\gamma) \end{bmatrix} \begin{bmatrix} A_{\theta n}^{b} \\ A_{\theta n}^{e} \end{bmatrix} \quad (14)$$

By substituting boundary condition $B_{zn}^{b}=0$ for (14)

$$A_{\theta n}^{b} = -\frac{G_0(\beta,\gamma)}{F_0(\gamma,\beta)} A_{\theta n}^{e} \quad (15)$$

By substituting (15) for (14)

$$B_{zn}^{e} = P_1 A_{\theta n}^{e} \quad (16)$$

By substituting boundary condition $B_{zn}^{h}=0$ for (13)

$$A_{\theta n}^{h} = \frac{1}{F_0(\gamma,\delta)} \left\{ \frac{N_2}{k_n^2} - G_0(\delta,\gamma) A_{\theta n}^{e} \right\} \quad (17)$$

By substituting (16) and (17) for (13), we can obtain the magnetic vector potential at the boundary surface *(e)*, namely, $A^{e}_{\theta n}$ as following:

$$A_{\theta n}^{e} = \frac{N_1 F_0(\gamma,\delta) - N_2 G_0(\gamma,\delta)}{P_1 F_0(\gamma,\delta) + k_n^2 \{F_0(\delta,\gamma) F_0(\gamma,\delta) - G_0(\delta,\gamma) G_0(\gamma,\delta)\}} \quad (18)$$

where the coefficients P_1, N_1 and N_2 are will be given in Appendix.

4.3 The generalization of vector potentials

In order to generalize the magnetic vector potentials due to PMs in the air-gap regions of Fig. 4, the transfer relations for the air-gap regions of Fig. 4 can be written by

$$\begin{bmatrix} B_{zn}^{R} \\ B_{zn}^{e} \end{bmatrix} = -k_n^2 \begin{bmatrix} F_0(\gamma,R) & G_0(R,\gamma) \\ G_0(\gamma,R) & F_0(R,\gamma) \end{bmatrix} \begin{bmatrix} A_{\theta n}^{R} \\ A_{\theta n}^{e} \end{bmatrix} \quad (19)$$

where R represents an imaginary boundary with the range of $\gamma \le R \le \beta$, as shown in Fig. 4. Using (16) and (19), the magnetic vector potential due to PMs at the imaginary boundary is given by

$$A_{\theta n}^{R(PM)} = \frac{-1}{G_0(\gamma,R)} \left\{ \frac{P_1}{k_n^2} + F_0(R,\gamma) \right\} A_{\theta n}^{e} \quad (20)$$

On the other hand, radial and axial component of

magnetic field distributions due to PMs are given by a definition of magnetic vector potential $\mathbf{B}=\nabla\times\mathbf{A}$ as followings:

$$B_{rn}^{R(PM)} = jk_n A_{\theta n}^{R(PM)} = \frac{-jk_n}{G_0(\gamma,R)}\left\{\frac{P_1}{k_n^2}+F_0(R,\gamma)\right\}A_{\theta n}^{e} \quad (21.a)$$

$$B_{zn}^{R(PM)} = \frac{A_{\theta n}^{R(PM)}}{r'}+\frac{\partial A_{\theta n}^{R(PM)}}{\partial r'} = \frac{A_{\theta n}^{R(PM)}}{R}+ k_n\gamma\left[\begin{array}{l} P_1\{X(R)K_1(k_n\gamma)-I_1(k_n\gamma)Y(R)\}- \\ k_n\left\{\dfrac{F(R,\gamma)g(R,\gamma)-f(R,\gamma)G(R,\gamma)}{g(R,\gamma)^2}\right\}\end{array}\right]A_{\theta n}^{e} \quad (21.b)$$

where the coefficients $F(R,\gamma)$, $f(R,\gamma)$, $G(R,\gamma)$, $g(R,\gamma)$, $X(R)$ and $Y(R)$ will also given in Appendix.

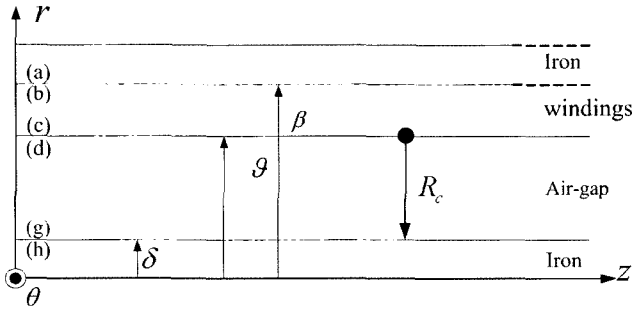

Fig. 6. Model for the generalization of vector potentials due to stator currents.

5. Fields due to stator currents

5.1 Boundary conditions

In case of prediction of magnetic fields due to stator currents, the PM regions are contained in air-gap regions by assumption that the relative recoil permeability for those is unity, as shown in Fig. 6. On the other hand, boundary conditions used in prediction of the magnetic field distributions due to stator currents are as followings:

I) $B_{zn}^{a}=0$ and $B_{zn}^{g}=0$ by assumptions that the permeability of the stator core and rotor shaft is infinite,

II) $B_{zn}^{a}-B_{zn}^{b}=0$ and $B_{zn}^{c}-B_{zn}^{d}=0$ because there is no surface current at upper and lower surface of winding regions,

III) $A_{\theta n}^{a}=A_{\theta n}^{b}$ and $A_{\theta n}^{c}=A_{\theta n}^{d}$ by continuity of vector potentials at all boundaries.

5.2 Vector potentials

By boundary conditions II) and III) presented in section 5.1, (10) can be rewritten by

$$\begin{bmatrix} B_{zn}^{a} \\ B_{zn}^{d}\end{bmatrix} = -k_n^2\begin{bmatrix} F_0(\vartheta,\beta) & G_0(\beta,\vartheta) \\ G_0(\vartheta,\beta) & F_0(\beta,\vartheta)\end{bmatrix}\begin{bmatrix} A_{\theta n}^{a} \\ A_{\theta n}^{d}\end{bmatrix}+\begin{bmatrix} J_1 \\ J_2\end{bmatrix} \quad (22)$$

Where

$$\begin{bmatrix} J_1 \\ J_2\end{bmatrix} = \mu_0 J_n\begin{bmatrix} F_0(\vartheta,\beta)+G_0(\beta,\vartheta) \\ G_0(\vartheta,\beta)+F_0(\beta,\vartheta)\end{bmatrix}$$

As shown in Fig. 6, since the air-gap regions contain the PM regions, the transfer relations of air-gap regions shown in Fig. 6 are given by

$$\begin{bmatrix} B_{zn}^{d} \\ B_{zn}^{g}\end{bmatrix} = -k_n^2\begin{bmatrix} F_0(\delta,\vartheta) & G_0(\vartheta,\delta) \\ G_0(\delta,\vartheta) & F_0(\vartheta,\delta)\end{bmatrix}\begin{bmatrix} A_{\theta n}^{d} \\ A_{\theta n}^{g}\end{bmatrix} \quad (23)$$

By substituting boundary condition $B_{zn}^{g}=0$ for (23)

$$A_{\theta n}^{g} = -\left(G_0(\delta,\vartheta)/F_0(\vartheta,\delta)\right)A_{\theta n}^{d} \quad (24)$$

By substituting (24) for (23)

$$B_{zn}^{d} = P_2 A_{\theta n}^{d} \quad (25)$$

By substituting boundary condition $B_{zn}^{a}=0$ for (22)

$$A_{\theta n}^{a} = \frac{1}{F_0(\vartheta,\beta)}\left\{\frac{J_1}{k_n^2}-G_0(\beta,\vartheta)A_{\theta n}^{d}\right\} \quad (26)$$

By substituting (25) and (26) for (22), the magnetic vector potential at boundary surface *(d)*, namely, $A^{d}{}_{\theta n}$ is given by

$$A_{\theta n}^{d} = \frac{-G_0(\vartheta,\beta)J_1+J_2F_0(\vartheta,\beta)}{F_0(\vartheta,\beta)\{P_2+P_3\}} \quad (27)$$

where the coefficients P_2 and P_3 are given by

$$P_2 = -k_n^2\left\{F_0(\delta,\vartheta)-\frac{G_0(\vartheta,\delta)G_0(\delta,\vartheta)}{F_0(\vartheta,\delta)}\right\} \quad (28.a)$$

$$P_3 = k_n^2 \left\{ F_0(\beta,\vartheta) - \frac{G_0(\vartheta,\beta)G_0(\beta,\vartheta)}{F_0(\vartheta,\beta)} \right\} \quad (28.b)$$

5.3 The generalization of vector potentials

In order to generalize the magnetic vector potentials due to stator currents in the air-gap regions of Fig. 6, the transfer relations for the air-gap regions are given by

$$\begin{bmatrix} B_{zn}^{d} \\ B_{zn}^{R_c} \end{bmatrix} = -k_n^2 \begin{bmatrix} F_0(R_c,\vartheta) & G_0(\vartheta,R_c) \\ G_0(R_c,\vartheta) & F_0(\vartheta,R_c) \end{bmatrix} \begin{bmatrix} A_{\theta n}^{d} \\ A_{\theta n}^{R_c} \end{bmatrix} \quad (29)$$

where R_c represents an imaginary boundary with the range of $\delta \le R_c \le \vartheta$. Using (25) and (29), the magnetic vector potential at the imaginary boundary is given by

$$A_{\theta n}^{R_c(coil)} = \frac{-1}{G_0(\vartheta,R_c)} \left\{ \frac{P_2}{k_n^2} + F_0(R_c,\vartheta) \right\} A_{\theta n}^{d} \quad (30)$$

As a consequence, radial and axial component of flux density due to stator currents are given by

$$B_{rn}^{R_c(coil)} = jk_n A_{\theta n}^{R_c(coil)} = \frac{-jk_n}{G_0(\vartheta,R_c)} \left\{ \frac{P_2}{k_n^2} + F_0(R_c,\vartheta) \right\} A_{\theta n}^{d} \quad (31.a)$$

$$B_{zn}^{R_c(coil)} = \frac{A_{\theta n}^{R_c(coil)}}{r} + \frac{\partial A_{\theta n}^{R_c(coil)}}{\partial r} = \frac{A_{\theta n}^{R_c(coil)}}{R_c} + k_n\vartheta \left[\begin{array}{l} P_2\{X(R_c)K_1(k_n\vartheta) - I_1(k_n\gamma)Y(R_c)\} - \\ k_n \left\{ \dfrac{F(R_c,\vartheta)g(R_c,\vartheta) - f(R_c,\vartheta)G(R_c,\vartheta)}{g(R_c,\vartheta)^2} \right\} \end{array} \right] A_{\theta n}^{d} \quad (31.b)$$

where the coefficients $F(R_c, \vartheta)$, $f(R_c, \vartheta)$, $G(R_c, \vartheta)$, $g(R_c, \vartheta)$, $X(R_c)$ and $Y(R_c)$ will also given in Appendix.

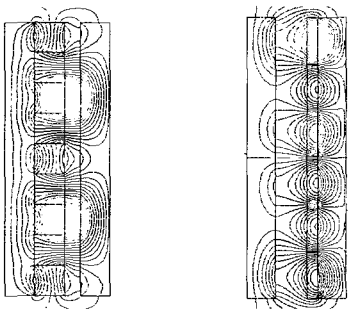

(a) (b)

Fig. 7. Magnetic flux distributions due to (a) PMs and (b) stator currents obtained by FE analyses.

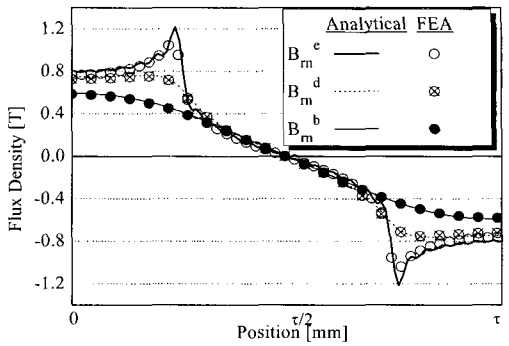

(a)

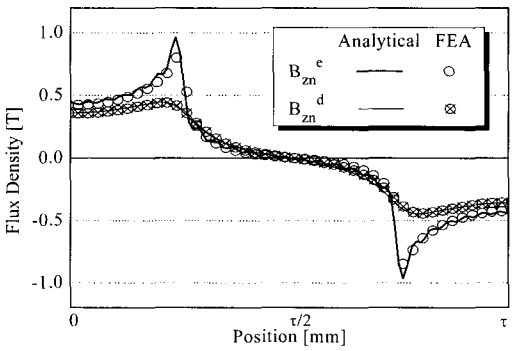

(b)

Fig. 8. Comparison of between analytical and FE results for (a) radial and (b) axial flux density due to PMs.

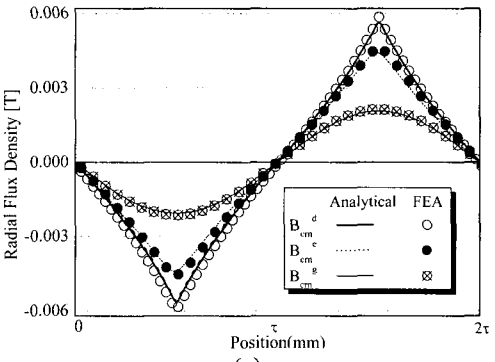

(a)

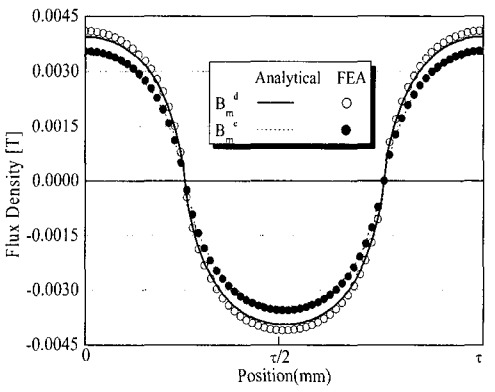

(b)

Fig. 9. Comparison of between analytical and FE results for (a) radial and (b) axial flux density due to stator currents.

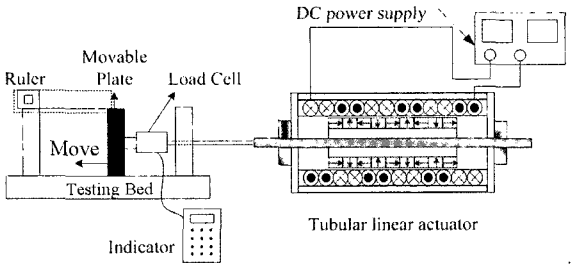

Fig. 10. Experimental systems for thrust measurements.

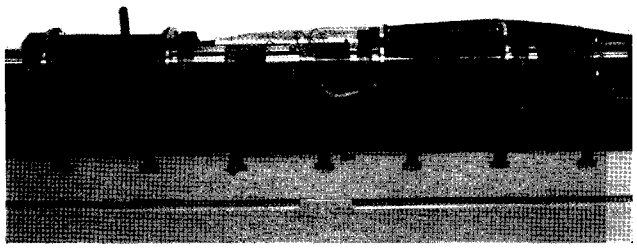

Fig. 11. Photograph for concept of back-emf measurements.

Table 1. Estimated Control Parameters of tubular linear actuator.

	Analytical	FEA	Experimental
Thrust constant K_T [N/A]	48	48	48
Back-emf constant K_E [V·s/m]	48	48	46
Inductance L [mH]	-	3.25	2.8
Resistance R [Ω]	6	6	6.1

6. Comparison of predictions with FE calculations

This chapter describes the comparison of predictions with FE calculations for flux density due to PMs and stator currents. A commercial package ANSOFT MAXWELL is employed for FE analyses. Fig. 7 shows the magnetic flux lines due to PMs and stator currents. Fig. 8 and 9 shows the comparison of between analytical and FE results for radial and axial flux density due to PMs and stator currents, respectively. All analytical results are in good agreement with those obtained from FE analyses. It can be observed from Fig. 8(a) and Fig. 9(a) that radial flux density due to PMs and stator currents is the most sinusoidal at the boundary surface (b) and (g), respectively.

7. Control Parameters

Fig. 10 shows the testing apparatus for measurements of thrust. As shown in Fig. 11, given that we manufactured two sets of tubular linear actuators, the back-emf is measured by the driving actuator as a generator at a given speed that depends on the speed of the other actuator driven as a motor [9]. Table 1 shows the control parameters of the tubular linear actuator obtained from the analytical, FE and experimental method. The analytical results are shown to be in good agreement with those obtained from measurements and FE analyses.

7.1 Thrust and back-emf constant

The thrust acting on the windings by interaction between the PMs and the winding currents is derived via the Maxwell stress tensor. If the radii of the magnet and current regions are large compared with their thickness, thrust equations for planar linear motors given in [5] can be employed for the prediction of thrust for tubular linear motor [4]. As presented in [5], the stress tensor T_{ij} for magnetically linear materials associated with the Korteweg-Helmholtz force density is

$$T_{ij} = \mu H_i H_j - \delta_{ij} \mu H_k H_k / 2 \tag{32}$$

where the Kronecker delta δ_{ij} is when $i \neq j$, and is 1 when $i = j$. By the Einstein summation convention and assumption that a volume of the winding on which the thrust acts encloses an integer number of periods[2], the thrust acting on the enclosed section of the winding is given by

$$\begin{aligned} F_z &= -S < T_{rz}^e >_z = -S\mu_0 < H_r^e H_z^e >_z \\ &= -S\mu_0 \sum_{n=-\infty}^{\infty} H_r^e \cdot \left(H_z^e\right)^* \end{aligned} \tag{33}$$

where the upper surface (boundary e) area of the PMs that encloses an integer number of periods is $S = 2p\tau w$, p is the pole-pairs of the mover and w is given by $2\pi\gamma$. H_r^e and H_z^e are radial and axial fields due to both the PMs and the winding currents at boundary surface (e), respectively and can be obtained by the sum of (21.a) and (31.a) and by the sum of (21.b) and (31.b), respectively. The superscripts * denotes complex conjugate. On the other hand, the thrust constant (K_T) can be calculated from (33) as following:

$$F_z = K_T i \tag{34}$$

where i is the phase current. The back-emf constant (K_E) can be calculated by

$$e_b = \frac{d\lambda^{PM}}{dt} = \frac{dz_0}{dt}\frac{d\lambda^{PM}}{dz_0} = v\frac{d\lambda^{PM}}{dz_0} = vK_E \tag{35}$$

where λ^{PM} represent a linkage flux passing the windings due to PMs and can be obtained by line integral of (20).

However, since (20) contains the Bessel functions, its integral causes analytical burden. However, generally, since the thrust constant is identical with the back-emf constant for the case when stator of the actuator has single-phase windings, we can predict back-emf constant from thrust constant calculated by the force equation of planar motor analytically. Fig. 12 (a) and (b) shows the comparison among analytical, FE and experimental results for the axial thrust according to mover position and the maximum value of back-emf according to mover velocity. The analytical results are shown to be in good agreement with those obtained from FE analyses and measurements. It can be predicted from Fig. 12(a) and (b) that both thrust constant and back emf constant are 48 approximately. It is noted that the analytical results shown in Fig. 12(b) is obtained from assumptions that the thrust constant is identical with the back-emf constant for the case when stator of the actuator has single-phase windings.

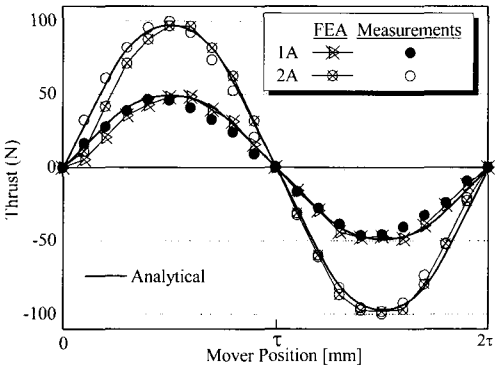

Fig. 12. Comparison among analytical, FE and experimental results for (a) the axial thrust according to mover position and (b) the back-emf according to mover velocity.

7.2 Resistance and Inductance

Since it can be assumed that the AC coil resistance of the windings is the same as the DC coil resistance, for the case when the actuator is driven at a low frequency, the resistance of the tubular linear actuator is calculated by [10]

$$R = \frac{4\rho_c N l_{1c}}{\pi d_c^2} \tag{36}$$

where ρ_c, d_c, N and l_{1c} denote resistivity, radius, turns and length of conductor, respectively. Fig. 13 shows the comparison among analytical, FE and measurements for the resistance. Since length of conductor l_{1c} in (36) is employed for depth of conductor model in 'transient mode' of the ANSOFT MAXWELL for FE analyses, analytical results obtained from (36) are shown to be in excellent agreement with FE results. On the other hand, the winding self inductance (L_s) is calculated by

$$\lambda^J = L_s i_s \tag{37}$$

where λ^J represent a linkage flux passing the windings due to stator currents and can be obtained by line integral of magnetic vector potential due to stator currents in winding regions. Although we do not calculate this analytically because of analytical burden such as integrals of Bessel functions, as shown in Fig. 14 and Table I, we can obtain this using FE analyses and measurements. In particular, PM6806 RCLmeter of the FLUKE is employed for inductance measurements.

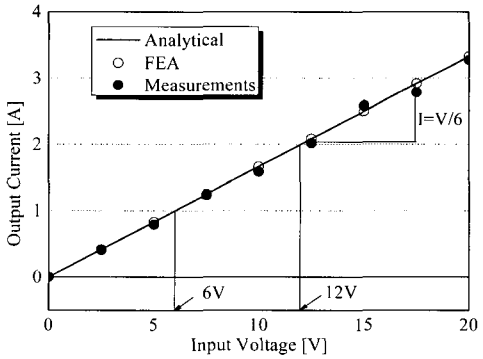

Fig. 13. Comparison among analytical, FE and experimental results for resistance.

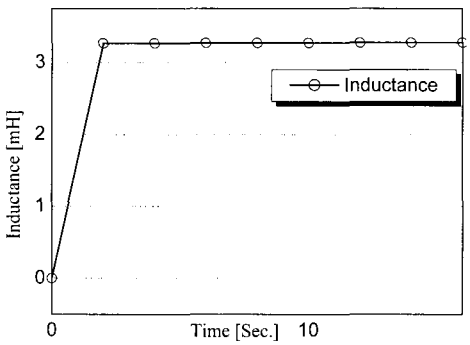

Fig. 14. FE results for inductance.

8. Conclusions

Analytical prediction for electromagnetic characteristics such as magnetic flux density due to PMs and thrust of tubular linear actuator with Halbach array using transfer relations has been described. The analytical results have been validated extensively with FE results. On the basis of 2-d analytical solutions, this paper has predicted control parameters such as thrust, back-emf constant and resistance of tubular linear actuator. Test results such as thrust, back-emf, inductance and resistance measurements are given to confirm electromagnetic analysis and control parameters estimated from analytical solutions. The predicted control parameters are shown to be in good agreement with those measured.

Appendix

- Derived Coefficients

$$N_1 = -\mu_0 \left[jk_n M_{rn} \left\{ F_0(\delta,\gamma) + G_0(\gamma,\delta) \right\} - M_{zn} \right]$$

$$N_2 = -\mu_0 \left[jk_n M_{rn} \left\{ G_0(\delta,\gamma) + F_0(\gamma,\delta) \right\} - M_{zn} \right]$$

$$P_1 = k_n^2 \left\{ \frac{G_0(\beta,\gamma) G_0(\gamma,\beta)}{F_0(\gamma,\beta)} - F_0(\beta,\gamma) \right\}$$

$$X(r) = -\frac{I_1(k_n r)}{k_n r} + I_0(k_n r)$$

$$Y(r) = -\frac{K_1(k_n r)}{k_n r} - K_0(k_n r)$$

$$f(a,b) =$$
$$I_1(k_n a)^2 K_1(k_n b) K_0(k_n b) + I_1(k_n a) K_1(k_n a) K_1(k_n b) I_0(k_n b)$$
$$-I_1(k_n a) K_1(k_n a) K_0(k_n b) I_1(k_n b) - K_1(k_n a)^2 I_1(k_n b) I_0(k_n b)$$

$$g(a,b) = K_1(k_n a) I_1(k_n b) - I_1(k_n a) K_1(k_n b)$$

$$F(x,y) = 2X(x) I_1(k_n x) K_1(k_n y) K_0(k_n y) +$$
$$\{X(x) K_1(k_n x) + Y(x) I_1(k_n x)\} \{K_1(k_n y) I_0(k_n y) - I_1(k_n y) K_0(k_n y)\}$$
$$-2Y(x) K_1(k_n x) I_1(k_n y) I_0(k_n y)$$

$$G(x,y) = Y(x) I_1(k_n y) - X(x) K_1(k_n y)$$

Acknowledgements

This work was financially supported by MOCIE through the IERC program, Korea.

References

[1] MASADA, E.: 'Linear drives for industrial applications in Japan history, existing state and future prospect'. Proceedings of LDIA'95, Japan, pp. 9-12.

[2] Jiabin Wang, Geraint W. Jewell and David Howe, "A General Framework for the Analysis and Design of Tubular Linear Permanent Magnet Machines", *IEEE Trans. Magn.*, vol. 35, no. 3, pp.1986-2000, May. 1999.

[3] J. Wang, G. W. Jewell and D. Howe, "Design optimization and comparison of tubular permanent magnet machine topologies", *IEE Proc.-Electr. Power Appl.*, vol. 148, no. 5, pp. 456-464, Sept. 2001.

[4] W.-J. Kim, M. T. Berhan, D. L. Trumper and J. H. Lang, "Design optimization and comparison of tubular permanent magnet machine topologies", in Conf. Rec. *IEEE-IAS 31th Annu. Meeting*, pp. 471-478, 1996.

[5] David L. Trumper, Won-jong Kim, and Mark E. Williams, "Design and Analysis Framework for Linear Permanent-Magnet Machines", *IEEE,Trans. IAS*, vol. 32, pp. 371-379, 1996.

[6] David L. Trumper and Mark E. Williams, "Halbach Arrays in Precision Motion Control", *The Art and Science of Magnet Design*, vol. 1, Feb. 1995

[7] Won-jong Kim, Bryan C. Murphy, "Development of a Novel Direct-Drive Tubular Linear Brushless Permanent-Magnet Motor", *IEEE Transactions on Industry Applications*, vol. 3, pp. 1664-1671, Oct. 2003.

[8] Nicola Bianchi, "Analytical Field Computation of a Tubular Permanent-Magnet Linear Motor", *IEEE Trans., Magn.*, vol. 36, pp. 3798-2801, 2000.

[9] J. R. Hendershot and TJE Miller, "*Design of Brushless Permanent Magnet Motors*", Magna Physics Publishing and Clarendon Press, 1994.

[10] Duane Hanselman, *Brushless Permanent Magnet Motor Design*. The Writer's Collective, 2003.

Seok-Myeong Jang

He was born in Korea in 1949. He received his B.E., M.S., and Ph.D. degrees from Hanyang University in 1976, 1978, and 1986, respectively. He is a professor in the Department of Electrical Engineering, Chungnam National University. He worked as a visiting researcher in the Department of Electrical Engineering, Kentucky University in 1989. He is a member of KIEE. His field of interest includes Design and Application of Linear Machines, High Speed Machines, and Linear Oscillating Actuator.

Jang-Young Choi

He was born in Korea in 1976. He received his B.S. and M.S. degrees in electrical engineering from Chungnam National University in 2003 and 2005, respectively. He is currently working toward his Ph.D. in the Department of Electrical Engineering at Chungnam National University. His research interests are design and analysis of linear and rotary PM machines.